Korean J. Chem. Eng., **28**(5), 1214-1220 (2011)
DOI: 10.1007/s11814-010-0503-1

Solar photocatalytic detoxification of cyanide by different forms of TiO_2

Chockalingam Karunakaran†, Paramasivan Gomathisankar, and Govindasamy Manikandan

Department of Chemistry, Annamalai University, Annamalainagar 608002, Tamilnadu, India
(*Received 12 April 2010 • accepted 2 December 2010*)

Abstract−The photocatalytic efficiencies of TiO_2 nanocrystals of different modifications (anatase, rutile, P25 Degussa, Hombikat), to oxidize cyanide ion and subsequently the cyanate also, under natural sunlight at 950±25 W m^{-2} in alkaline solution have been compared. The oxides have been characterized by powder XRD, UV-visible diffuse reflectance and impedance spectroscopies. Under identical solar irradiance, the reaction follows Langmuir-Hinshelwood kinetics on cyanide, and depends on the apparent area of the catalyst bed and dissolved oxygen. However, the adsorption of cyanide on TiO_2 in dark is too small to be measured analytically. The photocatalytic activity of TiO_2 is not solely governed by the band gap or charge-transfer resistance or capacitance or phase composition but is in accordance with the specific surface area or the average crystallite size; rutile is an exception.

Key words: Photooxidation, Sunlight, Specific Surface Area, Crystal Size, Kinetics

INTRODUCTION

Cyanide ion is a very toxic pollutant that originates from metal finishing and electroplating shops. Physical, chemical and biological methods can be used to remove the dissolved cyanide. The physical methods are based on ion exchange, adsorption or foam-flotation and can only transfer cyanide from one phase to another. The biodegradation is very slow and is limited to low concentration of cyanide. Further, it encounters the difficulty of disposal of the activated sludge. Among the chemical methods alkaline chlorination is the best available technique, but the limitations are the formation of highly toxic cyanogen chloride gas and the leftover complex metal cyanide in sludge. A promising method of detoxification of cyanide is the photocatalytic one and semiconductor-catalyzed oxidation of cyanide with artificial UV light is known; TiO_2 and ZnO are the catalysts used [1-7].

Illumination of semiconductor with light of energy not less than the band gap leads to formation electron-hole pairs, holes in the valence band and electrons in the conduction band [8]. A fraction of these pairs diffuse out to the surface of the crystal and participate in chemical reactions with adsorbed electron donors and acceptors resulting in photocatalysis. The photogenerated hole oxidizes the substrate and the electron is taken up by the adsorbed oxygen molecule yielding highly unstable superoxide radical, O_2^- [9]. With water, O_2^- in turn generates reactive oxygen species like HO, HO_2 and H_2O_2, which also oxidize the substrate. Water is adsorbed on the semiconductor surface, both molecularly and dissociatively [10,11]. Hole-trapping by either the surface hydroxyl groups or adsorbed water molecules results in short-lived HO radicals, which are the primary oxidizing agents [12-15]. Natural sunlight is available free of cost and utilization of the same is desirable in semiconductor-catalyzed environmental remediation. Studies on semiconductor-catalysis with natural sunlight are rare, probably due to the problem of fluctuation of solar irradiance during the experiment, and it has now been overcome by exposing the semiconductor beds to identical solar irradiance. The experiments have been carried out simultaneously, side by side. Even though several semiconductors like α-Fe_2O_3, CdO and CdS undergo band gap excitation with visible light [8] and exhibit photocatalytic activity, they are susceptible to photocorrosion and hence are unsuitable for environmental remediation. TiO_2 is chemically inert, tolerant to acidic and alkaline media, photostable, non-toxic, inexpensive, and reusable. The solar light harvesting efficiency of TiO_2 could be improved by doping. Doping TiO_2 with transition metal ions like Cu, Ni and Co slightly shifts its absorption edge to visible region and enhances the removal of cyanide [16,17]. Deposition of noble metals like Ag on TiO_2 also improves the cyanide degradation [17]. But, experiments show that the doped metal is eaten away by cyanide. The photocatalytic efficiency of the semiconductor depends on the competition between two processes, namely, the surface charge carrier transfer and the electron-hole recombination. Intrinsic parameters like crystal properties (particle size, surface area, crystal structure, point of zero charge, adsorption of hydroxyl ions and water molecules, etc.), optical properties (band gap, etc.) and electronic properties (charge-transfer resistance, capacitance, etc.) and extrinsic parameters like wavelength and intensity of illumination, catalyst loading, pH, temperature, dissolved oxygen, substrate concentration, etc., determine the photocatalytic efficiency of the semiconductor. Furthermore, the photocatalytic activity is substrate specific; a recent study with eight commercial TiO_2 samples and 19 test substrates confirms the same [18]. Here we compare the solar photocatalytic efficiencies of different forms of TiO_2 nanocrystals to detoxify cyanide and rationalize them in terms of their physicochemical parameters.

EXPERIMENTAL

1. Materials

TiO_2 P25 (Degussa), TiO_2 anatase (Sigma-Aldrich), TiO_2 rutile (Sigma-Aldrich) and Hombikat TiO_2 (Fluka) nanoparticles and TiO_2

†To whom correspondence should be addressed.
E-mail: karunakaranc@rediffmail.com

(Merck) submicron particles were used as supplied.

2. Characterization

The powder X-ray diffractograms of the titanium dioxides were recorded using a Siemens D-5000 XRD with Cu K_α X-rays of wavelength 1.5406 Å under a scan range of 5-60° at a scan speed of 0.2° s^{-1} or a Bruker D8 system using Cu K_α radiation of 1.5406 Å in a 2θ range of 5-70° at a scan speed of 0.050 s^{-1}. Rich Seifert model 3000 X-ray diffractrometer was also employed for the diffraction studies. JEOL JSM-5610 equipped with BE detector was the scanning electron microscope (SEM) used. The sample was placed on an adhesive carbon slice supported on copper stubs and coated with 10 nm thick gold using JEOL JFC-1600 auto fine coater prior to measurement. The surface area of the submicron particulate TiO_2 was determined with a Micromeritics ASAP 2020 sorption analyzer. The sample was degassed at 150 °C for 12 h and the analysis was conducted at −196 °C with N_2 as the adsorbate gas. The specific surface area was obtained by the Brunauer-Emmett-Teller (BET) multipoint method, through a least-square fit. A Perkin-Elmer Lamda 35 spectrophotometer was used to record the UV-visible diffuse reflectance spectra of the oxides. The impedance spectral data of different forms of TiO_2 crystals were obtained with a HP 4284A Precision LCR meter over the frequency range of 1 MHz to 20 Hz at room temperature in air [19]; while the disk area was 0.5024 cm^2 the thicknesses of anatase, rutile, P25, Hombikat nano TiO_2 and anatase submicron TiO_2 pellets were 2.12, 1.53, 2.78, 1.80, and 2.98 mm, respectively.

3. Method

The TiO_2-catalyzed solar photooxidation was made with AM 1 sunlight under clear sky in summer (March-July). The intensity of sunlight was measured by using a Daystar solarmeter (USA). In each experiment, the corresponding TiO_2 was taken along with fresh air-saturated KCN solution of desired ppm at pH 12.5 (using NaOH) and the TiO_2 particles were carefully allowed to settle down and cover uniformly the entire bottom of the wide cylindrical glass vessel prior to illumination. The TiO_2 bed was undisturbed till the completion of solar irradiance. After, and also prior to, solar illumination the cyanide ion was analyzed argentometrically using *p*-dimethylaminobenzylidene rhodanine as the indicator [17]. Spectrophotometric determination of cyanide ion at 590 nm by complexing it with ninhydrin in alkaline medium [20] also provided identical results. Cyanide ion analysis using cyanide ion selective electrode with Ag/AgCl electrode as the reference was also in accordance with the other two methods. Cyanate was analyzed spectrophotometrically [5]. The dissolved oxygen was measured with an Elico dissolved oxygen analyzer PE 135. Presonication of the dry catalyst, the catalyst slurry in cyanide solution or simultaneous sonication (sonication during solar irradiance) was made by using a Toshcon SW 2 ultrasonic bath (37±3 kHz, 100 W).

The photooxidation with UV light was carried out in a multilamp photoreactor fitted with 8 W mercury lamps of wavelength 365 nm (Sankyo Denki, Japan) and a highly polished anodized aluminium reflector. The reaction vessel was a borosilicate glass tube of 15-mm inner diameter and was placed at the center. The reaction tube was illuminated by four lamps with the angle sustained by the adjacent lamps at the sample as 90°. The four cooling fans at the bottom of the reactor dissipate the generated heat. The light intensity was determined by ferrioxalate actinometry [21]. 25 mL of KCN solution at pH 12.5 was purged with air that effectively kept the added TiO_2 under suspension and at continuous motion. The airflow rate was measured by the soap bubble method. Similar to the solar experiments, cyanide as well as cyanate was analyzed prior to and after illumination.

RESULT AND DISCUSSION

The powder XRD of TiO_2 anatase nanocrystals used confirms its structure; it matches with the standard JCPDS pattern of anatase TiO_2 (89-4921, tetragonal, body centred) and the rutile lines are absent. The XRD of rutile TiO_2 sample is in agreement with its crystal structure. The observed pattern matches the standard JCPDS pattern of rutile TiO_2 (89-4202, tetragonal, primitive) and the anatase lines are not seen. The X-ray diffractogram of the TiO_2 P25 used confirms the presence of anatase and rutile phases in the sample; the standard JCPDS patterns of anatase (00-021-1272) as well as rutile (01-089-0553 C) are observed. The phase percentages have been obtained from the integrated intensity of the peaks at 2θ value of 25.3° (101) for anatase and 27.4° (110) for rutile. The percentage of anatase is given by the formula, $A\ (\%)=100/\{1+1.265(I_R/I_A)\}$, where I_R is the intensity of the rutile peak at $2\theta=27.4°$ and I_A is that of the anatase peak at $2\theta=25.3°$. The phase composition thus determined is 81% anatase and 19% rutile, which is in agreement with that provided by the manufacturer. The XRD of Hombikat TiO_2 shows the presence of anatase as well as rutile phases; the peak fitting conforms to the JCPDS patterns of anatase (89-4921) and rutile (110, 211, etc., peaks). The percentages of anatase and rutile phases, obtained using the intensities of 101 peak of anatase and 110 peak of rutile, are 69 and 31, respectively. The XRD of the used TiO_2 submicron particles reveals the structure as anatase; the diffraction pattern totally matches with the standard pattern of anatase (JCPDS 01-078-2486 C, tetragonal, body centred). The average sizes of the nanocrystals have been obtained from the half-width of the full maximum (HWFM) of the most intense peaks of the different nanocrystals using the Scherrer equation, $D=k\lambda/\beta\cos\theta$, where D is the average crystallite size, λ is the X-ray wavelength, θ is the Bragg angle, β is the corrected half-peak width of the experimental sample and k is the shape factor of value 0.9. The specific surface area of the nanoparticles, listed in Table 1, has been obtained using the relationship, $S=6/\rho D$, where S is the specific surface area, D is the mean particle size and ρ is the material density. The specific surface area of TiO_2 submicron particles has been determined by the N_2-adsorption-desorption isotherms using the BET (Brunauer-Emmett-Teller) equation. The average particle size has been deduced from the determined BET surface area.

The band gaps of the oxides deduced from the Tauc plots (not shown) and listed in Table 1 are in agreement with the literature. The Tauc plots have been drawn using the F(R) values, obtained by the application of Kubelka-Munk algorithm to the measured diffuse reflectance data [22]. The deduced band gaps clearly reveal that all the TiO_2 samples require UV-A light for the photoexcitation. Impedance spectroscopy (IS) is a relatively new and powerful tool to probe the electrical properties of semiconductors [23]. It may be used to investigate the dynamics of the bound and mobile charges in the bulk or interfacial region of the semiconductors. In polycrystalline materials, the overall sample resistance may be a combination

Table 1. Crystal size (D), specific surface area (S), band gap (E_g), absorption edge (λ), ohmic (R_Ω) and charge-transfer (R_{CT}) resistances, and capacitance (C) of TiO_2

TiO_2	D, nm	S, $m^2\ g^{-1}$	E_g, eV	λ, nm	R_Ω, k_Ω	R_{CT}, k_Ω	σ, mS m^{-1}	C, pF
Anatase	9	163	3.22	385	12	41	1.03	9.7
Hombikat	16	92	3.16	392	9	203	0.18	8.2
P25 Degussa	23	66	3.14	395	4	37	1.50	43
Rutile	12	122	3.03	409	20	70	0.38	7.1
Anatase (submicron)	104	14.7	3.20	388	57	58	1.02	13.8

of the intragranular or bulk crystal resistance and intergranular or grain boundary resistance. Generally, the impedance data are analyzed in terms of an equivalent circuit model; an electrode interface undergoing an electrochemical reaction is typically analogous to an electric circuit consisting of a specific combination of resistors and capacitors. By fitting the IS data to a model or an equivalent circuit the electrochemical properties of the semiconductors may be inferred. The recorded impedance spectra (not given), the variation of impedance with frequency, of the different TiO_2 used show decrease of impedance with increase of frequency, indicating the capacitance of the semiconductors studied. The Nyquist plot, a popular format of evaluating the electrochemical impedance data, is presented in Fig. 1. The ohmic or uncompensated resistance (R_Ω) corresponds to the grain boundary or intergranular resistance and the polarization or electron-transfer (charge-transfer) resistance (R_P or R_{CT}) refers to the intragranular or bulk crystal resistance; the latter is related to the Warburg resistance, the resistance to mass transfer, which is controlled by the specific conductance, σ. The constant phase element (CPE) can be associated with a non-uniform distribution of current due to material heterogeneity and is equivalent to a double layer capacitance, C. Although P25 Degussa and Hombikat are the blends of anatase and rutile phases, they show single semicircles in the Nyquist plots, indicating homogeneity in the electrical properties of the materials. The Nyquist plot of Hombikat displays a large charge-transfer resistance with only a very limited frequency region where mass transfer is a significant factor, thus suggesting the predominance of kinetic control; the semiconductor may be photocatalytically sluggish. All other Nyquist plots show large regions of mass-transfer with significant kinetic control at low and high frequencies, respectively. Also, the large grain boundary resistance of the submicron particles could be inferred from the Nyquist plot. Table 1 presents the determined specific conductance, capacitance and the ohmic and charge-transfer resistances of the different forms of TiO_2 employed. The specific conductance has been deduced from the measured charge-transfer resistance, and the capacitance has been obtained using the equations $\omega_{max}=1/CR_{CT}$ and $\omega_{max}=2\pi f$, where f is the frequency corresponding to the maximum of the semicircular Nyquist plot. Among the nanocrystals, the specific conductance of anatase is larger than that of rutile. But the benchmark photocatalyst P25 Degussa, which is a blend of anatase (81%) and rutile (19%) phases, exhibits surprisingly higher specific conductance than anatase and rutile. However, Hombikat, which also contains anatase (69%) and rutile (31%) phases, does not show similar characteristics; its specific conductance is even less than that of rutile. Further, P25 Degussa exhibits the largest capacitance among the semiconductors examined.

The oxidation of cyanide ion under natural solar irradiance of 950±25 W m^{-2} at pH 12.5 is catalyzed by all the above-mentioned

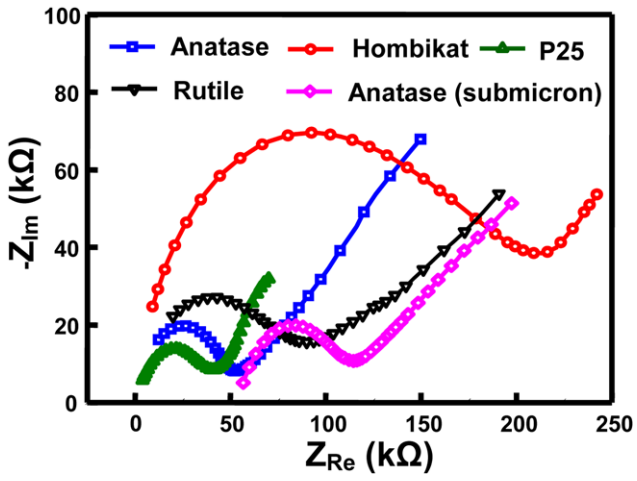

Fig. 1. The Nyquist plots.

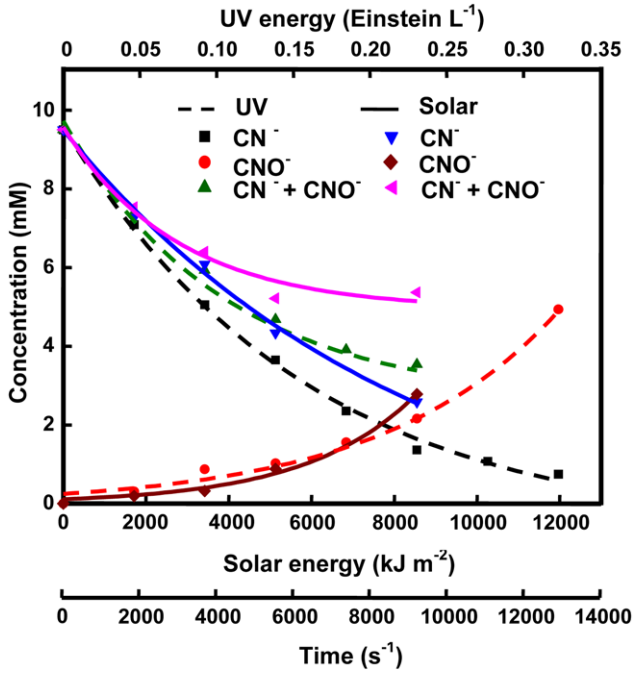

Fig. 2. The temporal profile of cyanide oxidation. Nanoparticulate anatase loading=0.100 g (solar, 16.7 cm^2 bed) or 0.020 g (UV), pH=12.5, $[O_2]_{dissolved}$=26.8 ppm, cyanide solution=25 mL; solar irradiance (11.00 am-2.30 pm): 950±25 W m^{-2}; UV: λ=365 nm, I=25.4 μEinstein L^{-1} s^{-1}, airflow rate=7.8 mL s^{-1}.

forms of TiO_2. The pK_a of HCN is 9.3, and to avoid its liberation into the atmosphere the detoxification has been made in a highly alkaline medium. Under identical conditions, cyanide ion is not oxidized in absence of TiO_2. Analysis of the cyanide solution after solar irradiance with different TiO_2 confirms the formation of cyanate at the expense of cyanide and this is in agreement with the literature [3-7]. Experiments with cyanate separately show that it is also oxidized under natural sunlight as well as under UV-A light, which is in line with the earlier reports; carbonate and nitrate are the products reported (data not given). Analysis of cyanide as well as cyanate during solar and UV illumination of cyanide solution shows simultaneous oxidation of cyanide and cyanate; Fig. 2 is the time course of the cyanide oxidation under solar and UV-A light.

Even under clear sky in summer the sunlight intensity fluctuated during the course of the experiment (950±25 W m^{-2}). Also, it varied from day to day. Now, to get analyzable solar results the sunlight irradiance in a set of experiments has been kept identical by carrying out the experiments simultaneously, side by side. The solar results obtained with each TiO_2 have been consistent. For each catalyst, a couple of experiments with sunlight under identical reaction conditions and carried out simultaneously, side by side, yielded results within ±5% (*vide infra* for the experimental conditions). Carrying out simultaneously a control experiment along with others under the required experimental conditions made possible the analysis of the solar results.

The influence of experimental conditions such as cyanide-concentration, area of the catalyst bed and dissolved O_2 on the TiO_2-catalyzed oxidation rate has been studied individually. The solar irradiance in each study has been kept identical by carrying out a set of experiments simultaneously, side by side. For example, the photoremoval of cyanide at different cyanide concentrations for a particular form of TiO_2 has been determined simultaneously, side by side. Under identical sunlight irradiance, the cyanide oxidation rates increase with its concentration as shown by Fig. 3. The variation of cyanide-removal rates with its concentration is characteristic of Langmuir-Hinshelwood kinetics, which is based on the adsorption of cyanide ion on the semiconductors [24]. But the adsorption of cyanide ion on TiO_2 in dark at pH 12.5, even at the highest concentration of cyanide ion employed, is too small to be measured analytically. In alkaline medium, adsorption of HO^- on the semiconductors leads to negatively charged surface, and this could be a reason for the insignificant adsorption of cyanide ion. However, the observed Langmuir-Hinshelwood kinetics indicates that cyanide ion gets adsorbed significantly on the illuminated photoactive semiconductor surfaces. The percentages of cyanide ion removed by anatase, Hombikat, P25, and rutile nanoparticles and anatase submicron particles in 2½ h from a 100 ppm cyanide solution are 96, 90, 90, 85, and 82, respectively (other conditions remain as in Fig. 3). As shown by Fig. 4, the photooxidation rates exhibit linear dependence on the apparent area of the catalyst bed ($100r^2$=93-96). This is also in agreement with the Langmuir-Hinshelwood model. The different forms of TiO_2 show sustainable photocatalytic activities. Recycling of the catalysts without any pre-treatment provides identical results (conditions remain unaltered). Cyanide detoxification requires dissolved oxygen. The photooxidation of cyanide does not occur in nitrogen-purged solution (25 mL 250 ppm cyanide, pH 12.5, 0.10-g catalyst loading, 16.7 cm^2 catalyst bed, 1.8 and 26.8 ppm dissolved O_2 in N_2- and air-saturated solutions, respectively, 950±25 W m^{-2} sunlight, 30 min (11.45 am–12.15 pm)). Generally, sonication effects surface and particle size modification of the catalyst [25] and the photocatalytic activity is susceptible to the surface and size modification of TiO_2 particles. However, presonication of either the dry catalysts or the catalyst slurries in cyanide solutions (for 10 min at 37±3 kHz and 100 W) fails to enhance the solar photocatalytic activities. Sonophotocatalysis, sonication during photocatalysis (sonication of the catalysts in cyanide solution under sunlight), also fails to improve the photocatalytic efficiencies (conditions as

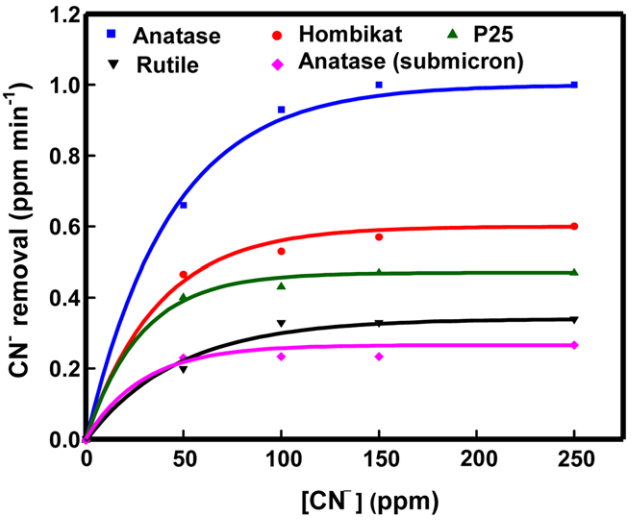

Fig. 3. Solar cyanide oxidation. The Langmuir-Hinshelwood kinetics.† Catalyst bed=16.7 cm^2, catalyst loading=0.100 g, pH=12.5, $[O_2]_{dissolved}$=26.8 ppm, illumination time=30 min (11.45 am–12.15 pm), solar irradiance=950±25 W m^{-2}, cyanide solution=25 mL. †Each catalysis corresponds to identical solar irradiance.

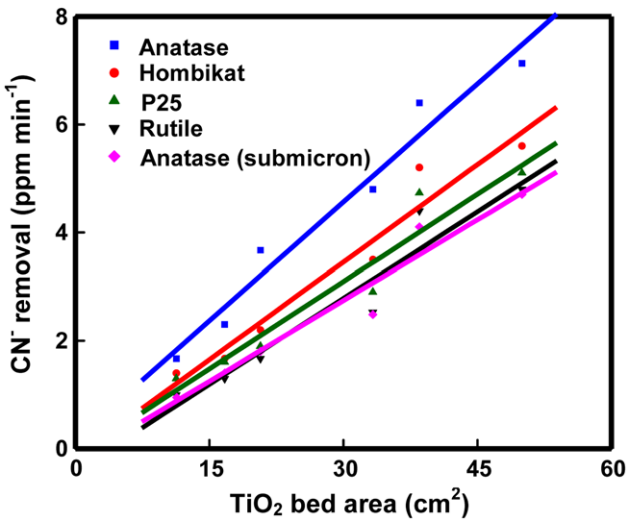

Fig. 4. Solar cyanide oxidation as a function of TiO_2 bed area.† Catalyst loading=0.100 g, pH=12.5, $[CN^-]_0$=250 ppm, $[O_2]_{dissolved}$=26.8 ppm, illumination time=30 min (11.45 am–12.15 pm), solar irradiance=950±25 W m^{-2}, cyanide solution=25 mL. †Each catalysis corresponds to identical solar irradiance.

in Fig. 3 with 250 ppm cyanide solution). However, the degradation of salicylic acid on Hombikat TiO_2 under UV light enhances on sonication [26]. Application of a potential bias to semiconductor under band gap-illumination reduces the recombination of the photogenerated electron-hole pairs and hence increases the photocatalytic efficiency [19,27-29]. However, in the present study, application of a potential bias (DC) fails to enhance the photooxidation of cyanide. Out of the four experiments conducted simultaneously in a set under identical solar irradiance for each catalyst, cost-effective stainless steel bottom has been used for three and the catalyst covered the entire bottom [19]. A positive potential bias has been applied for one, a negative potential to another and none to the third. Pt electrode (Elico) has been used as the counter electrode. The potential has been measured against SCE by using a potentiostat. Whether it is an anodic bias (+0.3 V vs NHE) or a cathodic bias (−0.1 V vs NHE), or no bias with TiO_2 on either glass bottom or stainless steel bottom, the cyanide ion removal remains unaltered under identical solar irradiance (25 mL 250 ppm cyanide, 12.5 pH, 26.8 ppm dissolved O_2, 0.10 g-catalyst loading, 16.7 cm^2 catalyst bed, 950±25 W m^{-2} sunlight for 2.5 h (11.00 am−2.30 pm)).

The Langmuir-Hinshelwood kinetic model is applicable to TiO_2-photocatalysis and the kinetic law is [24]:

$$\text{rate}=kK_1K_2IA[CN^-][O_2]/(1+K_1[CN^-])(1+K_2[O_2])$$

where K_1 and K_2 are the adsorption coefficients of cyanide ion and molecular oxygen on the illuminated surface of TiO_2, k is the surface pseudo-first-order rate constant, A is the surface area of the catalyst bed and I is the light intensity. The cyanide solutions are oxygen-saturated and the dissolved oxygen concentration has remained almost constant during the photooxidation. Since K_2 is a constant for a given catalysis $K_2[O_2]/(1+K_2[O_2])$ turns to be a constant for a given catalyzed oxidation. For a set of experiments conducted simultaneously I is a constant. The Langmuir-Hinshelwood kinetic model holds good as seen from the data fit to the curve governed by the Langmuir-Hinshelwood equation ($100r^2>98$) and drawn using a computer program (Fig. 3) and Table 2 presents the kinetic coefficients; the mechanism of photooxidation of cyanide on TiO_2 has been discussed elsewhere [3].

The UV light intensity in sunlight decreases from ~10 mEinstein m^{-2} h^{-1} at 400 nm to ~2.5 mEnistein m^{-2} h^{-1} at 325 nm and to zero at 300 nm. The intensity of impinging solar irradiance that leads to band gap excitation of TiO_2 of different modifications under identical solar irradiance, obtained from the determined band gap, decreases with increase of band gap energy. But the observed photocatalytic efficiencies under identical solar irradiance (experiments conducted simultaneously, side by side) increases with band gap energy suggesting that some other factor also operates (Fig. 5).

Table 2. The kinetic parameters

TiO_2	10^2 K_1, ppm^{-1}	10^3 $kK_2AI/(1+K_2[O_2])$, min^{-1}
Anatase	4.5	10.5
Rutile	2.4	3.9
P25 Degussa	7.1	4.4
Hombikat	8.0	5.8
Anatase (submicron)	5.0	2.7

Lower electron-transfer resistance should lead to a better separation of photogenerated electron-hole pairs. Hence it is reasonable to expect that the charge transfer resistance or specific conductance of the oxide reflects on its photocatalytic activity. But Fig. 5 does not show any such relationship. Further, the measured capacitances of the nanocrystals also do not reflect on the photocatalytic activities, indicating that the capacity of the semiconductor to hold charge is of little consequence in determining the photocatalysis. Hence, it is reasonable to state that the photodetoxification of cyanide by TiO_2 nanocrystals in alkaline solution is not governed by the resistance and capacitance of the crystals. The charge separation in the crystals is very fast and is not a controlling factor in cyanide oxidation. But a recent IS study on the Ag/TiO_2-photocatalyzed degradation of rhodamine B reveals a relationship between the photocatalytic activity and the charge-transfer resistance as well as the capacitance [30]. Of the 0.5% to 7% Ag-doped TiO_2 studied, the most active 3% Ag-doped TiO_2 shows the lowest charge-transfer resistance and highest capacitance. A similar study on the photodegradation of acid red 44 also supports such relationship [31]. While the reported photocatalytic activities are of the order TiO_2 nanospheres<TiO_2 nanorods<Ag-TiO_2 nanorods, the measured charge transfer resistances are as follows: TiO_2 nanospheres>TiO_2 nanorods>Ag-TiO_2 nanorods. The determined capacitances are in the order of the observed photocatalytic activities.

The TiO_2 crystals studied differ in their phase composition and the observed photocatalytic activities are not in agreement with the anatase content of the catalysts. Under UV-A light, anatase is more photoactive than rutile [9,32,33], and this is because of a larger photoabsorption and desorption of oxygen on the anatase surface and also to a lower electron-hole recombination [32]. Also, anatase is more active than rutile in adsorbing water and hydroxyl groups and the photocatalytic activity depends on the surface-adsorbed hydroxyl groups and water molecules [33]. Anatase blended with rutile is reported to show better photocatalytic performance than pure anatase due to enhanced separation of the photogenerated electron-hole pairs [34]. TiO_2 P25 Degussa (81% anatase, 19% rutile), a benchmarking photocatalyst, is reported to exhibit excellent activity due to synergistic effect between anatase and rutile phases; the charges produced on rutile by visible light are stabilized through rapid electron transfer from rutile to anatase, which thus extends the photoactivity into the visible region [35]. In the present study, TiO_2 Hombikat (69% anatase, 31% rutile) is more effective than TiO_2 P25 Degussa (81% anatase, 19% rutile) in detoxifying cyanide and the above proposition holds good. The rutile-anatase composition in Hombikat employed favors better charge separation than that in P25. However, these two anatase-rutile blends are only less active than pure anatase nanocrystals, indicating the operation of some other factors such as adsorption of O_2, H_2O and HO^-.

Examination of the observed cyanide detoxification under identical solar irradiance reveals that it is in agreement with the specific surface area of the different forms of TiO_2; rutile is an exception. Fig. 5 displays the variation of cyanide detoxification rates with specific surface area. Although the oxides of fixed mass are temporarily immobilized on glass surface to form a catalyst bed of the given apparent area, its actual surface area will be proportional to the specific surface area of the oxide. Furthermore, the crystal size determines the specific surface area and also plays an important role in

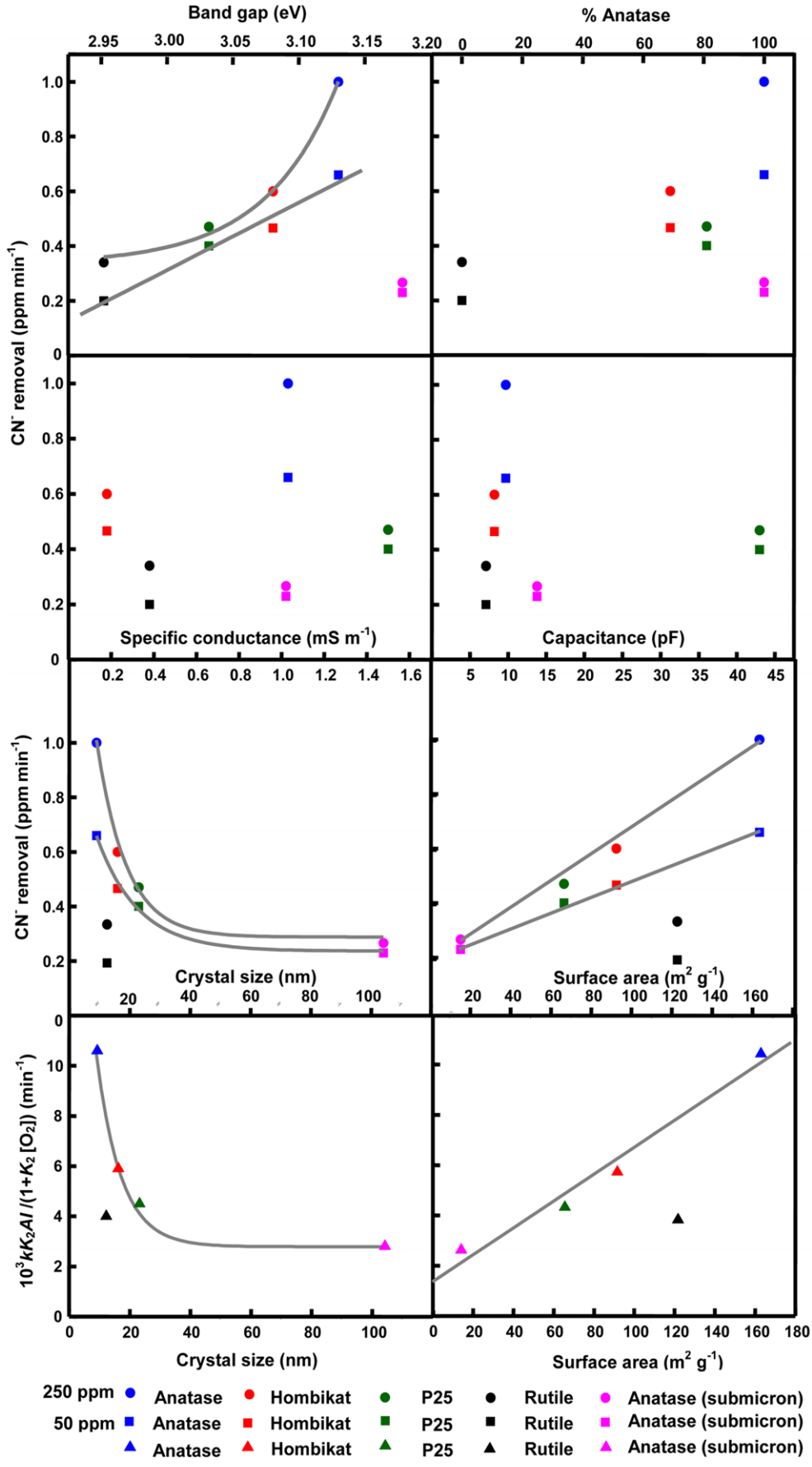

Fig. 5. Cyanide-photodetoxification and physicochemical parameters.

determining the photocatalytic activity: the smaller the size of the crystal, the higher is the photocatalytic activity. That is, the reactivity decreases with increase of the crystal size; rutile is an exception (Fig. 5). The surface trapping of electrons and holes may be more efficient in smaller crystals. The photogenerated electron-hole pairs have a much shorter distance to travel to reach the surface in smaller particles. Once the electrons and holes have been trapped at the interface, they can then participate in redox reactions. Similar results are observed with 10^3 $kK_2AI/(1+K_2[O_2])$, which reflects the surface pseudo-first-order rate constant of cyanide oxidation with specific surface area incorporated in it (Fig. 5).

CONCLUSIONS

With natural sunlight, different forms of TiO_2 effectively catalyze the oxidation of cyanide ion to cyanate ion; cyanate is also oxidized subsequently. Although the adsorption of cyanide ion on TiO_2 in dark is too small to be measured analytically, the photooxidation follows the Langmuir-Hinshelwood kinetics. The solar photocatalytic efficiencies of TiO_2 nanocrystals are of the order: anatase>Hombikat (69% anatase, 31% rutile)>P 25 Degussa (81% anatase, 19% rutile) >rutile>microparticulate anatase. The photocatalytic efficiency is not governed by the capacitance or charge-transfer resistance of the semiconductor but is in accordance with the specific surface area of the oxide; rutile is an exception.

ACKNOWLEDGEMENT

The authors thank the Council of Scientific and Industrial Research (CSIR), New Delhi, for the financial support through research grant no. 01(2031)/06/EMR-II and *Degussa* for gifting TiO_2 P25 sample. P.G. is grateful to CSIR for JRF. The authors also thank Dr. J. Jayabharathi for the DRS facility.

REFERENCES

1. J. Marugan, R. van Grieken, A. E. Cassano and O. M. Alfano, *Catal. Today*, **144**, 87 (2009).
2. J. Marugan, R. van Grieken, A. E. Cassano and O. M. Alfano, *Appl. Catal. B*, **85**, 48 (2008).
3. C. Karunakaran, in *Photo/Electrochemistry & Photobiology in the Environment, Energy and Fuel*, S. Kaneco Ed., Research Signpost, Trivandrum (2006).
4. A. Bozzi, I. Guasaquillo and J. Kiwi, *Appl. Catal. B*, **51**, 203 (2004).
5. K. Chiang, R. Amal and T. Tran, *J. Mol. Catal. A*, **193**, 285 (2003).
6. M. D. Hernandez-Alonso, J. M. Coronado, A. J. Maira, J. Soria, V. Loddo and V. Augugliaro, *Appl. Catal. B*, **39**, 257 (2002).
7. V. Augugliaro, V. Loddo, G. Marci, L. Palmisano and M. J. Lopez-Munoz, *J. Catal.*, **166**, 272 (1997).
8. R. Thiruvenkatachari, S. Vigneswaran and I. S. Moon, *Korean J. Chem. Eng.*, **25**, 65 (2008).
9. T. L. Thompson and J. T. Yates, Jr., *Chem. Rev.*, **106**, 4428 (2006).
10. R. Osgood, *Chem. Rev.*, **106**, 4379 (2006).
11. J. Zhao, B. Li, K. Onda, M. Feng and H. Petek, *Chem. Rev.*, **106**, 4402 (2006).
12. J. Peller, O. Wiest and P. V. Kamat, *J. Phys. Chem. A*, **108**, 10925 (2004).
13. Y. Shiraishi, N. Saito and T. Hirai, *J. Am. Chem. Soc.*, **127**, 12820 (2005).
14. Y. Du and J. Rabani, *J. Phys. Chem. B*, **107**, 11970 (2003).
15. L. Sun and J. R. Bolton, *J. Phys. Chem.*, **100**, 4127 (1996).
16. K. Chiang, R. Amal and T. Tran, *Adv. Environ. Res.*, **6**, 471 (2002).
17. H.-J. Kim, L. Lu, J.-H. Kim, C.-H. Lee, T. Hyeon, W. Choi and H.-I. Lee, *Bull. Korean Chem. Soc.*, **22**, 1371 (2001).
18. J. Ryu and W. Choi, *Environ. Sci. Technol.,* **42**, 294 (2008).
19. C. Karunakaran, P. Anilkumar, G. Manikandan and P. Gomathisankar, *Sol. Energy Mater. Sol. Cells*, **94**, 900 (2010).
20. P. Nagaraja, M. S. Hemanthakumar, H. S. Yathirajan and J. S. Prakash, *Anal. Sci.*, **18**, 1027 (2002).
21. H. J. Kuhn, S. E. Braslavsky and R. Schmidt, *Pure Appl. Chem.*, **76**, 2105 (2004).
22. S. Jung and J. H. Kim, *Korean J. Chem. Eng.*, **27**, 645 (2010).
23. A. J. Bard and L. R. Faulkner, *Electrochemical methods: Fundamentals and applications*, 2nd Ed., Wiley (2000).
24. C. Karunakaran, S. Senthilvelan and S. Karuthapandian, *J. Photochem. Photobiol. A*, **172**, 207 (2005).
25. K. Hirano, H. Nitta and K. Sawada, *Ultrason. Sonochem.*, **12**, 271 (2005).
26. E. P. Reddy, L. Davydov and P. Smirniotis, *Appl. Catal. B*, **42**, 1 (2003).
27. P. A. Christensen, T. A. Egerton, S. A. M. Kosa, J. R. Tinlin and K. Scott, *J. Appl. Electrochem.*, **35**, 683 (2005).
28. T. A. McMurray, J. A. Byrne, P. S. M. Dunlop and E. T. McAdams, *J. Appl. Electrochem.*, **35**, 723 (2005).
29. C. Karunakaran and P. Anilkumar, *Cent. Eur. J. Chem.*, **7**, 519 (2009).
30. B. Xin, Z. Ren, H. Hu, X. Zhang, C. Dong, K. Shi, L. Jing and H. Fu, *Appl. Surf. Sci.*, **252**, 2050 (2005).
31. H. J. Yun, H. Lee, N. D. Kim and J. Yi, *Electrochem. Commun.*, **11**, 363 (2009).
32. A. Sclafani and J. M. Herrmann, *J. Phys. Chem.*, **100**, 13655 (1996).
33. Z. Ding, G. O. Lu and P. F. Greenfield, *J. Phys. Chem. B*, **104**, 4815 (2000).
34. M. Yan, F. Chen, J. Zhang and M. Anpo, *J. Phys. Chem. B*, **109**, 8673 (2005).
35. D. C. Hurum, A. G. Agrios, K. A. Gray, T. Rajh and M. C. Thurnauer, *J. Phys. Chem. B*, **107**, 4545 (2003).